1-2005

Estimation of Gravity Wave Momentum Flux with Spectroscopic Imaging

Jing Tang

Farzad Kamalabadi

Steven J. Franke

Alan Z. Liu
Embry Riddle Aeronautical University - Daytona Beach, liuz2@erau.edu

Gary R. Swenson

Estimation of Gravity Wave Momentum Flux With Spectroscopic Imaging

Jing Tang, *Student Member, IEEE*, Farzad Kamalabadi, *Member, IEEE*, Steven J. Franke, *Senior Member, IEEE*, Alan Z. Liu, and Gary R. Swenson, *Member, IEEE*

***Abstract*—Atmospheric gravity waves play a significant role in the dynamics and thermal balance of the upper atmosphere. In this paper, we present a novel technique for automated and robust calculation of momentum flux of high-frequency quasi-monochromatic wave components from spectroscopic imaging and horizontal radar wind measurements. Our approach uses the two-dimensional (2-D) cross periodogram of two consecutive Doppler-shifted time-differenced (TD) images to identify wave components and estimate intrinsic wave parameters. Besides estimating the average perturbation of dominant waves in the whole field of view, this technique applies 2-D short-space Fourier transform to the TD images to identify localized wave events. With the wave parameters acquired, the momentum flux carried by all vertically propagating wave components is calculated using an analytical model relating the measured intensity perturbation to the wave amplitude. This model is tested by comparing wave perturbation amplitudes inferred from spectroscopic images with those from sodium lidar temperature measurements. The proposed technique enables characterization of the variations in the direction and strength of gravity waves with high temporal resolution for each clear data-taking night. The nightly results provide statistical information for investigating seasonal and geographical variations in momentum flux of gravity waves.**

***Index Terms*—Atmospheric measurement, feature extraction, spectrum analysis, spectroscopic imaging.**

I. Introduction

ATMOSPHERIC gravity waves (AGWs) are small-scale (tens to hundreds of kilometers in horizontal wavelength) wave perturbations of upper atmospheric constituent densities, winds, and temperatures. Generated by a variety of sources in the middle atmosphere and auroral regions, AGWs play a major role in the upper atmospheric dynamics and thermal balance by transporting and exchanging momentum and energy with the mean circulation. The vertical flux of horizontal momentum (per unit mass) is a vector quantity defined as the expected value of the product of the vertical wind perturbation and the horizontal wind perturbations. Usually, the momentum flux is represented by its orthogonal components in zonal and meridional directions, $\langle w'u' \rangle$ and $\langle w'v' \rangle$, with w' being the vertical wind perturbation, u' and v' the zonal and meridional wind perturbations, and the angle brackets denoting ensemble averaging. The net vertical transport effect by dissipating gravity waves is quantified by the divergence of the momentum flux. Using spectroscopic imaging to measure momentum flux will contribute to the understanding of gravity wave processes and their influence on global circulation.

Manuscript received December 29, 2003; revised July 26, 2004. This work was supported in part by the National Science Foundation under Grants ATM 99-08598, ATM 00-03182, and ATM 01-35073 and in part by the National Aeronautics and Space Administration under Grant NAG 5-10072 to the University of Illinois.

The authors are with the Department of Electrical and Computer Engineering and the Coordinated Science Laboratory, University of Illinois at Urbana-Champaign, Urbana, IL 61801 USA (e-mail: jingtang@uiuc.edu).

Digital Object Identifier 10.1109/TGRS.2004.836268

II. Related Work

Gravity wave momentum flux has been measured using radar, lidar, and spectroscopic airglow imaging systems. Ground-based radar or lidar systems employ two or more radar/lidar beams each offset from the vertical direction to measure the atmospheric motions with the Doppler technique [1]–[5]. Provided that the atmospheric motions are horizontally homogeneous within the beam coverage, the momentum flux is proportional to the difference of the variances of the Doppler velocities measured in each beam (see [1, eq. (5)]). Dual-beam radar and lidar observations have yielded important data on momentum flux and the associated mean flow acceleration. However, construction and operation of radar/lidar systems with necessary measurement accuracy, resolution, and beam-steering capabilities is expensive. Therefore, airglow imaging systems provide an attractive alternative for momentum flux measurement.

Spectral analysis has been used to process airglow images and estimate gravity wave features [6]–[8]. Several techniques have been reported for measuring wave momentum flux using airglow imaging systems. One technique presented by Gardner *et al.* [9] uses the azimuthal distribution of the relative airglow intensity as a proxy for the azimuthal distribution of the horizontal velocity variance. The measured variance distribution is used in the canonical power-law spectrum model [10] to predict the momentum flux as a function of azimuth angle. This technique estimates the momentum flux associated with both the monochromatic and quasi-random wave perturbations with 4-min to 2-h periods. As it does not identify individual waves, the technique does not determine whether the waves are vertically propagating. In addition to the spectral shape assumption, this technique also assumes that the variance spectra are separable in azimuth and intrinsic frequency. For scaling the correlation coefficients $\langle w'u' \rangle / (w'_{\rm rms} u'_{\rm rms})$ and $\langle w'v' \rangle / (w'_{\rm rms} v'_{\rm rms})$, derived from airglow images, to determine the momentum flux magnitudes, this technique requires high-resolution zenith and off-zenith lidar wind data for zonal, meridional, and vertical wind variance ($u'_{\rm rms}$, $v'_{\rm rms}$, and $w'_{\rm rms}$) calculation. Compared to airglow images, which can be taken in low-moon period of every month, the high-resolution lidar wind data are not readily available, and this fact puts limitations on the application of this technique. For example, observations made in 2002 and 2003 from Maui, HI, provide lidar wind data for only $\sim$20 nights, while airglow image data exist for 292 nights.

Another technique developed by Swenson *et al.* [11] and Haque and Swenson [12] is based on a model [13] relating the measured intensity perturbation to the relative atmospheric density perturbation and consequently to the gravity wave amplitude. For calculating momentum flux, quasi-monochromatic waves are identified and their wavelengths are measured from time-differenced (TD) image sequences. Block-motion analysis is employed for extracting the observed phase speed. Background horizontal wind data is required for gravity wave intrinsic phase speed calculation. As the investigation of seasonal and geographical variations of momentum flux requires significant processing, the technique employed by Swenson *et al.* [11] is impractical. The demand for processing large amounts of data prompts the necessity of developing an automated and robust technique.

III. New Technique

A technique has been developed to detect and identify high-frequency quasi-monochromatic wave components (wave period less than $\sim$40 min) and estimate intrinsic wave parameters from all-sky airglow images and background horizontal winds provided by any suitable technique (i.e., radar or lidar). Similar to the technique presented by Haque and Swenson [12], we use the Swenson and Liu [14] model (derived from [13]) for momentum flux estimation. The new technique corrects for the Doppler effect using three consecutive images and generates two TD images. The cross periodogram of the two TD images is processed in an effort to identify quasi-monochromatic wave components persisting in the three images and subsequently estimate their parameters including horizontal wavenumbers, intrinsic phase speeds, propagation directions, and wave perturbation energy. To identify localized wave components in the field of view (FOV), the two-dimensional (2-D) short-space Fourier transform (SSFT) is used for locating the portion that contains the largest energy content. Vertical wavelengths of the wave components are calculated using a gravity wave dispersion relation, and this resolves whether the waves propagate vertically before momentum flux calculations [15].

A. Image Preprocessing

Before TD images are produced for wave detection and wave parameter estimation, airglow images need to go through the following steps. First, we perform flat-fielding and interpolate the all-sky images to a uniform curvilinear grid of data points to correct the coordinate distortion from the fish-eye lens in the optical imaging system [16]. Second, stars are attenuated from the images using an edge-detection based technique [17]. Third, large-scale horizontal waves (e.g., tides) that can distort the low wavenumber region of periodogram are eliminated by detrending the data, which involves fitting a plane to the 2-D image data and then subtracting the fitted plane from the image.

In order to extract the intrinsic phase speed of a gravity wave from the observed wave motion, the background wind effect needs to be corrected. The wind velocity for the time when each image was taken can be estimated from lidar or radar horizontal wind measurement. In our case, the winds measured by a colocated radar are weighted by a perturbed hydroxyl (OH) profile to match the images taken by an OH imager [18]. We group three consecutive images and use the second image as a base. For the first image in the sequence, the pixels are shifted to the wind direction by the distance that wind traveled in the time interval between the acquisition of two images. For the third image, the pixels are repositioned against the wind direction. This process can also eliminate wave structures drifting with wind. It is hard to remove ripple structures that appear in regions of wind shear. However, as ripple structures occur in short periods of time and limited regions, they contribute little to the momentum flux budget.

B. Wave Detection and Intrinsic Phase Speed Estimation

After the above procedures are performed, two TD images are generated by taking the difference of pixel intensities between two consecutive images. The 2-D Fourier transform (FT) is then applied to the two TD images to acquire two periodograms and a cross periodogram [19, ch. 7–9, pp. 115–233]. A 2-D Hanning window with equivalent energy of a rectangular window of the same width is applied to the TD images before the periodograms are computed in order to minimize the sidelobe leakage and conserve the energy for sinusoidal wave components within a certain wavelength range.

Let $J_1(k,l)$ and $J_2(k,l)$ denote the FTs of the two TD images with k and l representing the wavenumbers in zonal and meridional directions, respectively. The periodogram of TD image 1 denoted by $I_{1,1}(k,l)$ is

$$I_{1,1}(k,l) = \frac{1}{n^2}|J_1(k,l)|^2 \tag{1}$$

where n^2 is the number of pixels in the TD image. $I_{2,2}(k,l)$ is defined similarly. The cross periodogram is given by

$$I_{1,2}(k,l) = \frac{1}{n^2}J_1(k,l)J_2^*(k,l) \tag{2}$$

where the asterisk designates complex conjugate. The squared magnitude of the cross periodogram

$$|I_{1,2}(k,l)|^2 = I_{1,1}(k,l)I_{2,2}(k,l) \tag{3}$$

is used to identify common wave components in the period when the three images were taken. The squared magnitude of the cross periodogram is an estimate of the product of the two TD images' power spectral densities. A peak detection algorithm is devised to seek local maxima in the squared magnitude of the cross periodogram (a typical one is shown in Fig. 1). The largest peak corresponds to the strongest quasi-monochromatic wave perturbation, which we call the dominant wave. Here, we use the term quasi-monochromatic to refer to a wave component with its frequency representation having a peak with surrounding pixel values dropping monotonically. The horizontal wavelength and the wavefront direction (azimuth) are calculated easily from the position of the peak. The wave propagation direction, which is perpendicular to the wavefront, is determined with a 180° ambiguity. In addition to the dominant wave, waves that have energy above 10% of the total energy in the periodograms, which can be distinguished from noise, also have their wavelengths and propagation directions estimated. Numerical simulations were used to determine the threshold of 10%, which provides a high probability of detecting a quasi-monochromatic wave and a negligible probability of incorrectly identifying a noise peak as a wave component.

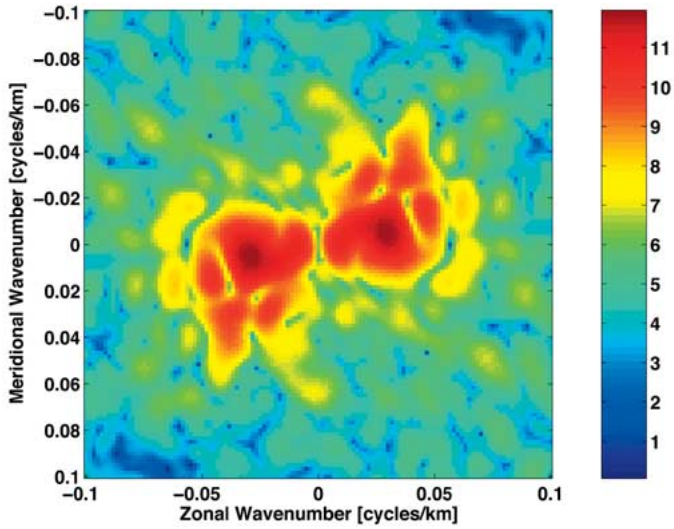

Fig. 1. Squared magnitude of the cross periodogram (in log scale) at 11–11.1 UT, July 9, 2002, Maui, HI.

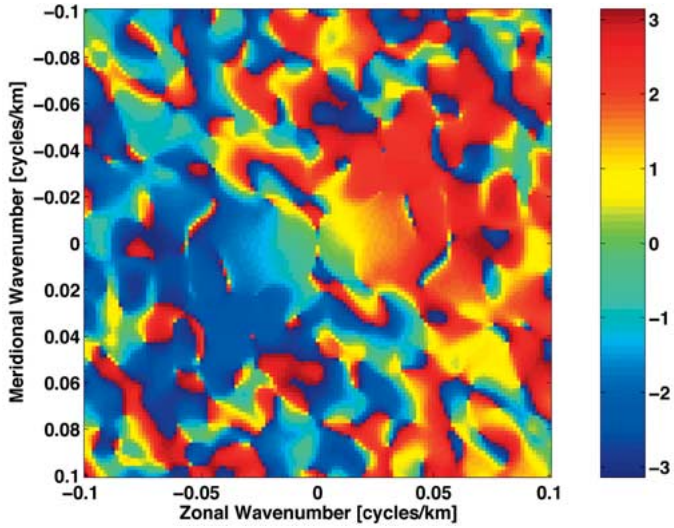

Fig. 2. Phase of the cross periodogram in Fig. 1.

The phase of the cross periodogram (a typical one shown in Fig. 2), equal to the difference of the phases in the two periodograms (or the relative phase), is employed for phase speed calculation. The phase at the maximum peak of the cross periodogram is the phase change caused by the propagation of the dominant wave. Therefore, with the wavelength known, the phase speed is readily computed. The wave propagation direction ambiguity (the two peaks symmetric to the origin have the same phase magnitude but opposite signs) is resolved assuming that a gravity wave recognized here does not travel more than half its wavelength in the time interval between two consecutive images (2 min, in our case), which is smaller than the wave period. The positive phase peak represents the real wave propagation direction. The phase velocities of wave components other than the dominant wave are obtained similarly.

C. Intensity Perturbation Estimation

The disturbed component of airglow intensity is estimated from the wavenumber domain analysis when TD images are used and undisturbed intensity is removed. The energy of a wave perturbation is the summation of the pixel values in the wave

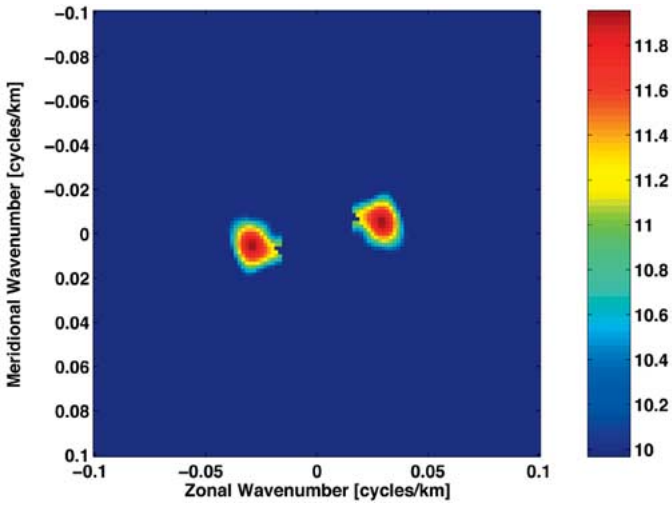

Fig. 3. Cross periodogram in Fig. 1 with dominant wave areas defined.

area from the periodogram. To define the wave area surrounding a wave peak, an algorithm is created to search the cross periodogram for pixels with values greater than 1% of the peak value (determined by simulating ideal sinusoidal waves based on wave energy conservation) on a spiral trace with the peak as the center. The algorithm also ensures that the wave area does not include pixels from other wave components through monotonicity checking. The cross periodogram with only the dominant wave area shown for Fig. 1 is presented in Fig. 3. In this specific case, the dominant wave contains 59% of the total energy in the TD images. The dominant wave perturbation energy extracted from the periodograms (of the whole FOV) is based on the assumption that the wavenumber content is uniform over the entire image. However, movies made from sequences of TD images reveal that the wave structures are not of even strength in the FOV. The extracted energy of wave components, therefore, is considered to be the average energy over the entire FOV.

Since in different regions a wave component has disparate strength, we divide the image into smaller overlapping sections and process each of them separately. To implement this idea, the SSFT is employed [20]. The SSFT of a 2-D signal $x(n_1, n_2)$ is given by

$$X(n_1, n_2, k, l) = \sum_{m_1} \sum_{m_2} x(m_1, m_2) \cdot w(n_1 - m_1, n_2 - m_2) e^{-j(km_1 + lm_2)} \quad (4)$$

where $w(n_1, n_2)$ is the 2-D analysis window, and k and l are the zonal and meridional wavenumbers, respectively. The 2-D SSFT can be interpreted as a set of FTs obtained by sliding the analysis window (in two dimensions) over the original image and taking FT of the product at each new position (see Fig. 4). Thus, the analysis window divides the original image into separate but overlapping sections. From the periodograms of all the overlapping sections, the one with the largest energy content of the wave component is selected and the wave perturbation energy is recovered from the periodogram. It is well known that the window size affects the SSFT analysis result. For waves with different wavelengths, we separate them into several ranges for choosing appropriate window sizes. The choice of window size is a compromise between the energy recovery ratio and the section size assumed to contain a uniform wave pattern. The energy recovery ratio of a

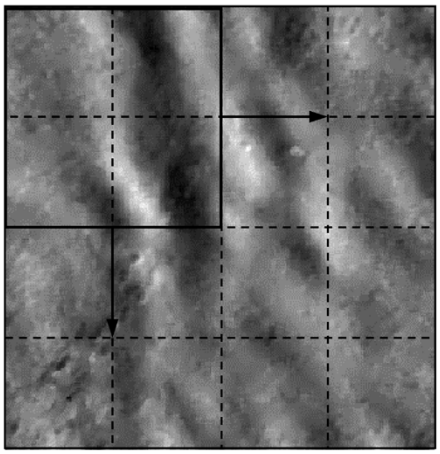

Fig. 4. Illustration of using SSFT on a TD image. The arrows represent the moving directions of the analysis window.

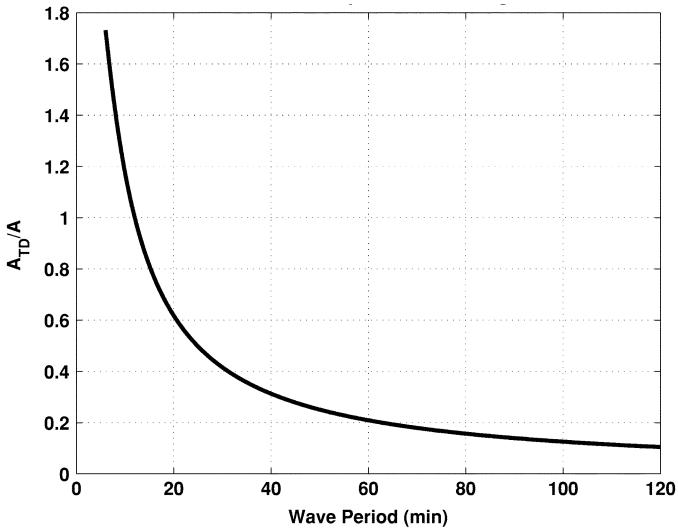

Fig. 5. Ratio of wave amplitude in a TD image (A_{TD}) to that in the original images (A) versus wave period with $\Delta t = 2$ min.

perturbation is defined as the ratio of the energy calculated from the wavenumber domain to the energy contained in the perturbation. The more perturbation cycles a window size contains, the closer the energy recovery ratio is to 1.

Regardless of whether the whole or partial FOV is used, the estimated value of the perturbed intensity (and, therefore, the wave amplitude) from a TD image must be mapped to a corresponding value in the original images. The ratio between the original wave amplitude and the Doppler-shifted TD wave amplitude is deduced by modeling an ideal sinusoidal wave. Suppose a sinusoidal wave in the second original image is represented by

$$E_1 = A\cos(kx - \omega_o t + \phi_0) \tag{5}$$

where A is the wave amplitude, k is the horizontal wavenumber, ω_o is the observed angular frequency, and ϕ_0 is the initial wave phase angle. With the Doppler wind correction applied to the third original image, the wave turns into

$$E_2 = A\cos(k(x + \Delta x) - \omega_o(t + \Delta t) + \phi_0) \tag{6}$$

where Δx is the distance wind travels in time interval Δt. Then the wave in Doppler-shifted TD image is given by

$$E_2 - E_1 = 2A\sin\left(\frac{\omega_o\Delta t - k\Delta x}{2}\right) \cdot \sin\left(k\left(x + \frac{\Delta x}{2}\right) - \omega_o\left(t + \frac{\Delta t}{2}\right) + \phi_0\right). \tag{7}$$

Therefore, the ratio of wave amplitude in the Doppler-shifted TD image to that in the original images is

$$\begin{aligned}\frac{A_{\mathrm{TD}}}{A} &= 2\left|\sin\left(\frac{\omega_o\Delta t - k\Delta x}{2}\right)\right| \\ &= 2\left|\sin\left(\frac{\Delta t(\omega_o - kv)}{2}\right)\right| \\ &= 2\left|\sin\left(\frac{\omega_i\Delta t}{2}\right)\right|\end{aligned} \tag{8}$$

where v is the wind speed and $\omega_i = \omega_o - kv$ is the intrinsic angular frequency of the wave. For waves with different intrinsic frequency (period) this ratio varies. When the time interval is too small compared with the wave period, the wave amplitude ratio is smaller than a discernible level. This results in a situation where the wave energy calculated from the cross periodogram is not significant to be recognized (refer to Section III-B). From Fig. 5, we see that the time-differencing process is for identifying high-frequency waves, i.e., mostly waves with period from 6 min (corresponding to three images, which is the unit for two TD image generation) to 20 min with the wave amplitude ratio A_{TD}/A between 1.732 and 0.618.

To calculate the intensity perturbation ratio, the intensity of the undisturbed airglow layer before the TD operation is needed. The charge-coupled device dark current and optical background in airglow emission are removed before the average of pixels in the star-free and detrended images can be taken as the undisturbed component of the intensity.

D. Momentum Flux Calculation

We use the Swenson and Liu model [14] to estimate monochromatic wave component momentum flux

$$F_M = \frac{g^2}{N^2}\frac{k}{m\cdot \mathrm{CF}^2}\left(\frac{I'}{\bar{I}}\right)^2 (\mathrm{m}^2\cdot\mathrm{s}^{-2}) \tag{9}$$

where g is the acceleration of gravity, N is the Brunt Vaisala (buoyancy) frequency, $k = 2\pi/\lambda_h$ is the horizontal wavenumber, λ_h is the horizontal wavelength, $m = 2\pi/\lambda_z$ is the vertical wavenumber, λ_z is the vertical wavelength, CF is the cancellation factor, and $I'/\bar{I}$ is the relative intensity perturbation. The cancellation factor relates the measured relative airglow intensity perturbation to the relative atmospheric density perturbation and consequently to the wave amplitude [18].

The vertical wavelength of a monochromatic gravity wave is related to its horizontal wavelength and intrinsic frequency through the dispersion relation

$$m^2 = \frac{N^2 - \omega^2}{\omega^2 - f^2}k^2 + \frac{\omega^2}{c_s^2} - \frac{1}{4H^2} \tag{10}$$

where ω is the intrinsic frequency, f is the inertial frequency, c_s is the local sound speed, and H is the scale height. Whenever m^2, calculated from known wave parameters, is negative, λ_z is imaginary, which suggests that the wave may be evanescent [15].

TABLE I
PARAMETERS OF A PERSISTENT WAVE EVENT FROM 12.8 TO 13.8 UT ON JULY 9, 2002, MAUI, HI, IDENTIFIED FROM IMAGER DATA USING THE PROPOSED TECHNIQUE

Time	Azimuth Angle (degree)	Intrinsic Wave Speed (m/s)	Wavenumber (1/km)	Horizontal Wavelength (km)	Vertical Wavelength (km)	Intrinsic Wave Period (min)	Observed Wave Period (min)	Wave Perturbation (%)
12.8	347.7	85.0	0.0144	69.3	31.0	13.6	21.1	4.8
12.9	351.5	99.5	0.0156	63.9	39.7	10.7	17.0	4.9
13.0	346.9	104.0	0.0166	60.3	43.8	9.7	14.6	5.9
13.1	350.5	91.2	0.0218	45.8	40.3	8.4	14.3	6.4
13.2	349.6	97.6	0.0223	44.9	47.1	7.7	12.2	4.6
13.3	350.7	88.0	0.0234	42.8	39.6	8.1	13.4	3.4
13.4	354.0	83.1	0.0219	45.6	34.2	9.2	17.7	3.1
13.5	358.8	84.1	0.0222	45.0	35.2	8.9	14.5	4.3
13.6	360.8	80.9	0.0222	45.1	32.9	9.3	16.3	3.8
13.7	369.2	82.7	0.0248	40.3	36.7	8.1	11.0	2.3
AVG	354.0	89.6	0.0205	50.3	38.1	9.4	15.2	4.3

IV. WAVE PERTURBATION VALIDATION

As suggested by the momentum flux equation (9), the wave perturbation term is the most important factor among wave parameters as its contribution is squared. The intensity perturbation estimated by the proposed technique is validated using the temperature perturbation extracted from the lidar measurement, since both the wave intensity perturbation and the temperature perturbation are related to the relative atmospheric density perturbation through the cancellation factors.

In the night of July 9, 2002, an OH airglow imager was operated at Maui, HI, while a colocated sodium (Na) lidar was collecting high-resolution (average one data point every 1.8 min) temperature data. A persistent wave event appears in both imager and lidar data from 12.8 to 13.8 universal time (UT). As shown in Table I, the wave has an observed period ranging from 11–21 min. We analyzed the spectral structure of the lidar temperature (integrated for OH layer) in this time interval and filtered the wave component. The rotational temperature perturbation $(T'_{\mathrm{R}}/T_{\mathrm{R}})$ caused by this wave is 0.78%.

Based on the model study presented in [18], for this specific wave with average vertical wavelength being 38.1 km, the cancellation factors representing the ratios of the airglow intensity perturbation to density perturbation and rotational temperature perturbation to density perturbation are calculated to be 4.1 and 0.8, respectively. Therefore, from the intensity perturbation extracted (from imager data), which is 4.3%, the density perturbation is estimated to be $4.3\%/4.1 = 1.1\%$. At the same time, the density perturbation is calculated to be $0.78\%/0.8 = 0.97\%$ from the rotational temperature perturbation (derived from lidar data). These two density perturbation results are comparable when two factors are considered. The first factor is related to the spatial variability of gravity waves. The lidar beam pointing straight to the zenith direction covers a small area ($\sim$35-m-diameter range), while the FOV of processed images is 150×150 km^2. The second factor is that the cancellation factors are calculated using the nominal atomic oxygen density. The atomic oxygen is a key constituent in the chemical production of OH emission, whose density varying from low to high changes the cancellation factor up to 20% in the vertical wavelength range this particular wave falls into [13].

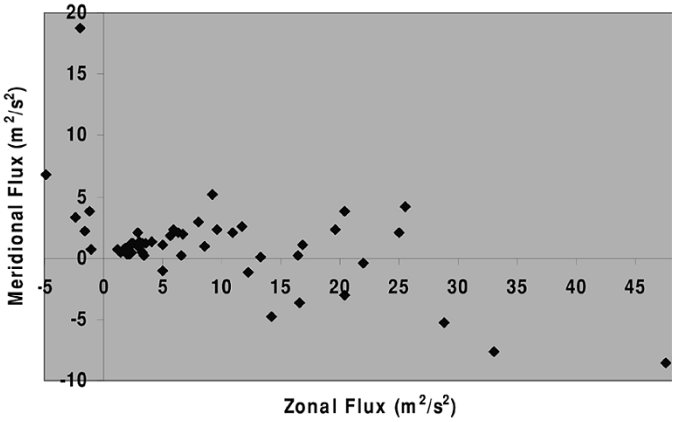

Fig. 6. Scatter plot of momentum fluxes on July 9, 2002, Maui, HI. Every point represents the momentum flux carried by all propagating wave components within a 6-min time interval.

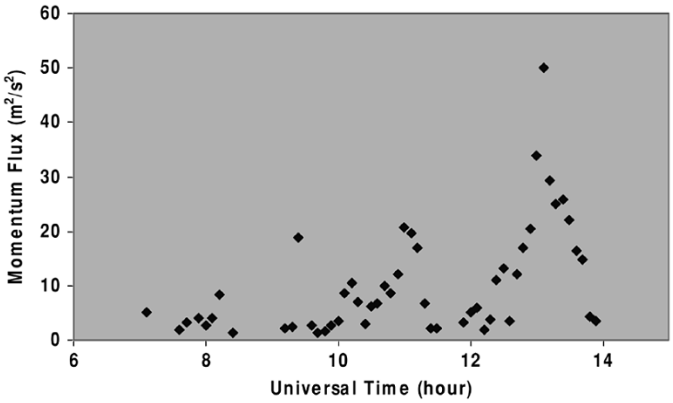

Fig. 7. Momentum flux magnitude variation over the night of July 9, 2002, Maui, HI.

V. EXPERIMENTAL RESULTS

Using the proposed technique, OH airglow imager data taken from Maui, HI has been processed. Here, we present data from the night of July 9, 2002 as an example. First, the average perturbations and momentum flux of recognizable quasi-monochromatic wave components over the whole FOV in every three consecutive images are calculated. Wave components with perturbation energy less than 10% of the energy in the entire periodograms are disregarded because the algorithm cannot distinguish them from noise. In every group of three images, the momentum flux estimation is the vector summation of the momentum fluxes of all the vertically propagating wave compoments. The scatter plot with every point representing momentum flux of all wave components in a 6-min interval is shown in Fig. 6 and the momentum flux magnitude variation versus time is presented in Fig. 7. The scatter plot of momentum flux shows that most of the wave components are propagating to the northeast, which coincides well with the wave propagation directions viewed in the TD image movie. From the

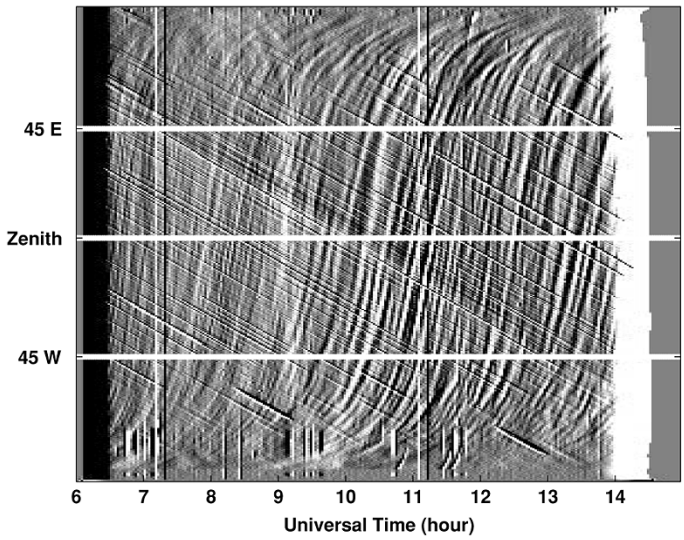

Fig. 8. East–west keogram on July 9, 2002, Maui, HI. It is generated by taking a horizontal column from the center of individual TD images and putting the columns side by side sequentially.

TABLE II
STATISTICS OF DOMINANT WAVE COMPONENTS ON JULY 9, 2002, MAUI, HI

Dominant Components	Average	Standard Deviation
Phase Speed (m/s)	80.5	14.3
Horizontal Wavelength (km)	47.6	21.8
Vertical Wavelength (km)	36.3	8.35
Wave Period (min)	9.98	4.99

	Entire Field of View		Maximum Perturbation Window	
	Average	Standard Deviation	Average	Standard Deviation
Wave Perturbation (%)	2.61	1.38	4.06	1.74
Zonal Flux (m^2/s^2)	9.22	11.1	21.2	29.1
Meridional Flux (m^2/s^2)	0.33	3.42	4.20	12.9
Total Flux (m^2/s^2)	10.4	10.5	28.2	26.1

movie and also the east–west keogram made by sequentially concatenating horizontal slices from the center of the TD images (shown in Fig. 8), stronger wave events happened after 10 UT. This is well reflected in the momentum flux magnitude plot. Second, the strongest portions of the dominant waves are selected using analysis windows, and corresponding intensity perturbations are calculated. The wave perturbation acquired in the strongest portion is considerably larger than its counterpart, which represents the average over whole FOV (Table II). (Note the average momentum flux magnitude is calculated from the flux in zonal and meridional directions; therefore, it represents the statistical result for the night.) The SSFT analysis shows that the observed wave events may exhibit significant amplitude variation within the imaging FOV. Further study of the amplitude variations may help to understand more about high-frequency quasi-monochromatic wave properties.

VI. SUMMARY

A novel approach for estimating high-frequency gravity wave momentum flux from spectroscopic airglow images is introduced. This proposed approach attempts to identify quasi-monochromatic wave components with time integration corresponding to three consecutive images and extracts wave parameters from the cross periodogram of two TD images. Since the images are Doppler corrected based on wind measurements, wave structures drifting with wind are removed before wave component identification. Moreover, the wave phase speeds determined from the phase of the cross periodogram are the intrinsic speeds. Since the method isolates high-frequency wave spectrum, no assumption regarding the spectral shape of total horizontal wind component is required. As each wave is considered individually, we can ensure it is not evanescent or ducted before the momentum flux calculation. Wave perturbations are estimated over the whole FOV and also in the strongest portion for recognizing localized waves. This method offers the possibility of investigating the daily variation of wave events as well as the seasonal and geographical variations of high-frequency gravity wave momentum flux.

By following the wavelengths (in zonal and meridional directions) and phase speeds of the wave components through a night, we observe some persistent wave components. More work is currently in progress toward identifying persistent wave events so that we can infer the properties of wave sources. Correlating the intensity perturbation estimated from imager data with the temperature perturbation from lidar measurements will contribute to the improvement of the model of cancellation factor. It may be possible to apply the proposed technique to images from different airglow emission layers to estimate the momentum flux divergence for a more complete understanding of the dissipation processes of high-frequency gravity waves.

ACKNOWLEDGMENT

The authors would like to acknowledge the constructive comments on this manuscript from all three reviewers.

REFERENCES

[1] R. A. Vincent and I. M. Reid, "HF Doppler measurements of mesospheric gravity wave momentum fluxes," *J. Atmos. Sci.*, vol. 40, no. 5, pp. 1321–1333, May 1983.

[2] I. M. Reid and R. A. Vincent, "Measurements of mesospheric gravity wave momentum fluxes and mean flow accelerations at Adelaide, Australia," *J. Atmos. Terr. Phys.*, vol. 49, no. 5, pp. 443–460, May 1987.

[3] X. Tao and C. S. Gardner, "Heat flux observations in the mesopause region above Haleakala," *Geophys. Res. Lett.*, vol. 22, no. 20, pp. 2829–2832, Oct. 1995.

[4] R. M. Worthington and L. Thomas, "The measurement of gravity wave momentum flux in the lower atmosphere using VHF radar," *Radio Sci.*, vol. 31, no. 6, pp. 1501–1517, Nov.–Dec. 1996.

[5] T. Nakamura, T. Tsuda, R. Maekawa, M. Tsutsumi, K. Shiokawa, and T. Ogawa, "Seasonal variation of gravity waves with various temporal and horizontal scales in the MLT region observed with radar and airglow imaging," *Adv. Space Res.*, vol. 27, no. 10, pp. 1737–1742, 2001.

[6] J. H. Hecht, R. L. Walterscheid, and M. N. Ross, "First measurement of the two-dimensional horizontal wave number spectrum from CCD images of the nightglow," *J. Geophys. Res.*, vol. 99, no. A6, pp. 11 449–11 460, June 1994.

[7] M. J. Taylor and F. J. Garcia, "A two-dimensional spectral analysis of short period gravity waves imaged in the OI (557.7 nm) and near infra red OH nightglow emissions over Arecibo, Puerto Rico," *Geophys. Res. Lett.*, vol. 22, no. 18, pp. 2473–2476, Sept. 1995.

[8] F. J. Garcia, M. J. Taylor, and M. C. Kelley, "Two-dimensional spectral analysis of mesospheric airglow image data," *Appl. Opt.*, vol. 36, no. 29, pp. 7374–7385, Oct. 1997.
[9] C. S. Gardner, K. Gulati, Y. Zhao, and G. R. Swenson, "Measuring gravity wave momentum fluxes with airglow imagers," *J. Geophys. Res.*, vol. 104, no. D10, pp. 11903–11 915, May 1999.
[10] D. C. Fritts and T. E. van Zandt, "Spectral estimates of gravity wave energy and momentum fluxes, part I: Energy dissipation, acceleration, and constraints," *J. Atmos. Sci.*, vol. 50, no. 22, pp. 3685–3694, Nov. 1993.
[11] G. R. Swenson, R. Haque, W. Yang, and C. S. Gardner, "Momentum and energy fluxes of monochromatic gravity waves observed by an OH imager at Starfire Optical Range, New Mexico," *J. Geophys. Res.*, vol. 104, no. D6, pp. 6067–6080, Mar. 1999.
[12] R. Haque and G. R. Swenson, "Extraction of motion parameters of gravity-wave structures from all-sky OH image sequences," *Appl. Opt.*, vol. 38, no. 21, pp. 4433–4442, July 1999.
[13] G. R. Swenson and C. S. Gardner, "Analytical models for the responses of the mesospheric OH^* and Na layers to atmospheric gravity waves," *J. Geophys. Res.*, vol. 103, no. D6, pp. 6271–6294, Mar. 1998.
[14] G. R. Swenson and A. Z. Liu, "A model for calculating acoustic gravity wave energy and momentum flux in the mesosphere from OH airglow," *Geophys. Res. Lett.*, vol. 25, no. 4, pp. 477–480, Feb. 1998.
[15] C. O. Hines, "Internal atmospheric gravity waves at ionospheric heights," *Can. J. Phys.*, vol. 38, pp. 1441–1481, 1960.
[16] S. B. Mende, R. H. Eather, and E. K. Aamodt, "Instrument for the monochromatic observation of all sky auroral images," *Appl. Opt.*, vol. 16, no. 6, pp. 1691–1700, June 1977.
[17] J. Tang, F. Kamalabadi, L. G. Rumsey, and G. R. Swenson, "Point-source suppression for atmospheric wave extraction from airglow imaging measurements," *IEEE Trans. Geosci. Remote Sensing*, vol. 41, pp. 146–152, Jan. 2003.
[18] A. Z. Liu and G. R. Swenson, "A modeling study of O_2 and OH airglow perturbations induced by atmospheric gravity waves," *J. Geophys. Res.*, vol. 108, no. D4, pp. 4151–4159, Feb. 2003.
[19] P. Bloomfield, *Fourier Analysis of Time Series: An Introduction*. New York: Wiley.
[20] S. H. Nawab and T. F. Quatieri, "Short-Time Fourier Transform," in *Advanced topics in signal processing*. ser. Prentice-Hall Signal Processing Series, J. S. Lim and A. V. Oppenheim, Eds. Engelwood Cliffs, NJ: Prentice-Hall, 1988, pp. 289–337.

Jing Tang (S'01) received the B.S. and M.S. degrees in measurement technique and instruments from Hefei University of Technology, Hefei, China, in 1993 and 1996, respectively. She is currently pursuing the Ph.D. degree in electrical and computer engineering at the University of Illinois, Urbana-Champaign.

Her research interests are mainly in the development of optical remote sensing techniques, signal and image processing, and atmospheric dynamics.

Ms. Tang received a China Instrument Scholarship in 1995. In 2004, she received a National Science Foundation Coupling, Energetics, and Dynamics of Atmosphere Regions workshop poster competition honorable mention.

Farzad Kamalabadi (M'02) received the B.S. degree in computer systems engineering from the University of Massachusetts, Amherst, in 1991, and the M.S. and Ph.D. degrees in electrical engineering from Boston University, Boston, MA, in 1994 and 2000, respectively.

He is currently an Assistant Professor in the Department of Electrical and Computer Engineering, University of Illinois, Urbana-Champaign. He was a Visiting Fellow with SRI International, in fall 2002, and a National Aeronautics and Space Administration (NASA) Faculty Fellow with the Jet Propulsion Laboratory, California Institute of Technology, in summer 2003. His research interests are in the development of optical and radio remote sensing and imaging techniques; atmospheric, ionospheric, and space physics; signal, array, and image processing; and signal reconstruction, estimation, and tomography.

Dr. Kamalabadi received an NSF Fellowship in 1994, a Best Student Paper Award in 1997, a NASA Fellowship in 1998, and an NSF Faculty Early Career Development (CAREER) Award in 2002. He has served in various organizational capacities, including Session Organizer and Chair for the International Union of Radio Science, special sessions on Ionospheric Imaging in 2003 and 2004.

Steven J. Franke (S'79–M'84–SM'90) was born in Chicago, IL on November 13, 1957. He received the B.S., M.S., and Ph.D. degrees in electrical engineering from the University of Illinois, Urbana-Champaign, in 1979, 1981, and 1984, respectively.

He is currently a Professor in the Department of Electrical and Computer Engineering, University of Illinois. He has published more than 100 refereed journal papers in the areas of acoustic wave propagation in the atmosphere, ionospheric wave propagation, ionospheric tomography, and remote sensing of the middle and upper atmosphere using radar techniques. He has served as Associate Editor of *Radio Science*.

Dr. Franke is an Associate Editor for IEEE ANTENNAS AND WIRELESS PROPAGATION LETTERS.

Alan Z. Liu received the B.S. degree in meteorology and the M.S. degree in atmospheric dynamics from Beijing University, Beijing, China, in 1987 and 1990, respectively, and the Ph.D. degree from the University of Illinois, Urbana-Champaign, in atmospheric sciences in 1996.

He joined the Electro-Optics System Laboratory, Department of Electrical and Computer Engineering, University of Illinois, Urbana-Champaign, in 1997 as a Research Scientist. His primary research area is using remote sensing methods, including lidar and airglow, to study the middle atmosphere dynamics and aeronomy. One of his main research interests is in the dynamics and effects of gravity waves in the middle atmosphere.

Dr. Liu is a member of the American Geophysical Union and the American Meteorology Society.

Gary R. Swenson (M'98) received the B.S. degree in mathematics and physics from Wisconsin State University, Superior, in 1963, and the M.S. and Ph.D. degrees in atmospheric science from the University of Michigan, Ann Arbor, in 1968 and 1975, respectively.

He is currently a Professor of electrical and computer engineering at the University of Illinois, Urbana-Champaign, where he is involved in remote sensing of the upper atmosphere using passive imaging and spectroscopy as well as lidar methods. He has worked at the National Aeronatics and Space Administation Marshall Space Flight Center from 1968 to 1983 in space environment and magnetospheric groups that included remote sensing of the upper atmosphere from ground-based as well as space shuttle experiments. He has also worked to characterize shuttle glow from spectroscopic measurements. From 1983 to 1996, he has worked at Lockheed Palo Alto Research Laboratory, Palo Alto, CA, in an atmospheric emissions group, primarily on instrumentation and measurements made from space shuttle of atmospheric airglow, aurora, as well as spacecraft glow. He was the Principal Investigator for the EISG experiment flown on STS62, which studied vehicle glows.

Dr. Swenson is a member of the American Geophysical Union and the American Institute of Aeronautics and Astronautics.

.